



1 **ABSTRACT:**

2 The strong metal-support interaction (SMSI) for supported Ni/CeO<sub>2</sub> catalysts with  
3 different CeO<sub>2</sub> nanomorphologies was systematically explored. The degree of  
4 encapsulation of Ni particles originating from the SMSI effect was found to follow the  
5 trend of Ni/CeO<sub>2</sub>-(111) > Ni/CeO<sub>2</sub>-(100) > Ni/CeO<sub>2</sub>-(110+100), which parallels the CO<sub>2</sub>  
6 hydrogenation activity. Quasi *in situ* XPS reveals the presence of Ce<sup>3+</sup> sites in accordance  
7 with the formation of an amorphous surface CeO<sub>x</sub> layer encapsulating the Ni  
8 nanoparticles. *In situ* DRIFTS indicates the reaction pathway and rate-determining step  
9 are dependent on the degree of the SMSI effect, leading to distinct selectivities towards  
10 CH<sub>4</sub>, especially at a high weight hourly space velocity (WHSV). These findings present a  
11 fundamental strategy about tailoring catalytic performance through support facet  
12 dependent susceptibility of SMSI phenomena.

13

14 **KEYWORDS:** *strong metal-support interaction, ceria, CO<sub>2</sub> methanation, nickel catalyst*

15

## 1 1. INTRODUCTION

2 The mitigation of CO<sub>2</sub> as a major greenhouse gas from anthropogenic emission has  
3 becoming a global initiative [1–3]. Hydrogenation of CO<sub>2</sub> yields fuels and commodity  
4 chemicals that plays an essential role in carbon neutrality and future sustainability [4–6].  
5 Among the various catalysts, supported nickel catalysts have received significant  
6 attention for catalyzing CO<sub>2</sub> hydrogenation due to their promising activities towards CH<sub>4</sub>  
7 production, a highly favored reaction compatible with the existing natural gas  
8 infrastructure [7]. Designing nickel-based catalysts with low-temperature activity,  
9 stability and fine-tuned product selectivity are key characteristics for industrial scale  
10 application that requires an in-depth understanding of their structure-activity relationship  
11 during the CO<sub>2</sub> methanation reaction [8–11].

12 Ceria is a versatile support material in heterogeneous catalysis with unique redox  
13 properties [12]. Previous studies reveal that CO<sub>2</sub> adsorption and activation is favored on  
14 oxygen vacancies of CeO<sub>2</sub> [13,14]. Furthermore, the strong metal-support interactions  
15 (SMSI), which often result in encapsulation of the stabilized nanoparticles (NPs) by the  
16 support, have been found for various CeO<sub>2</sub> supported catalysts that significantly impacted  
17 the catalytic performance [15,16]. For example, SMSI is commonly observed for the  
18 supported Ni/CeO<sub>2</sub> catalyst system with small Ni nanoparticles (~5 nm) under strong  
19 reducing environments [17,18]. In contrast, a recent work by Yuan *et al.* shows negligible  
20 SMSI phenomenon is found with larger metallic Ni particles (~11 nm) on CeO<sub>2</sub> during

1 the reverse water gas shift (RWGS) reaction [19]. Apparently, the SMSI effect is either  
2 environmental or morphological sensitive. On the other hand, a series of research works  
3 also reveal that tuning the facets of the support can be an effective approach for  
4 controlling metal support interactions and the resulting catalytic performance [20,21].  
5 Tang *et al.* reports the oxidative induced SMSI on Pd/TiO<sub>2</sub> is dependent on the facets of  
6 TiO<sub>2</sub> support. The Pd NPs supported on TiO<sub>2</sub> (101) and (100) surfaces are more  
7 susceptible to encapsulation of TiO<sub>x</sub> layer, which possess superior activities in methane  
8 combustion reaction [22]. However, in the Ni/CeO<sub>2</sub> system for CO<sub>2</sub> methanation, the  
9 fundamentals of such an interaction between Ni particles and CeO<sub>2</sub> support, as well as its  
10 correlation with the CO<sub>2</sub> methanation performance, have not been elucidated.

11 Herein, we systematically investigated the SMSI effect between metallic Ni  
12 nanoparticles and CeO<sub>2</sub> supports with various nanomorphologies / preferred facets under  
13 both hydrogen atmosphere and CO<sub>2</sub> methanation reaction conditions. The dynamic  
14 surface reconstruction process was revealed by a series of (quasi) *in situ* characterizations.  
15 A correlation between surface reduction / adsorption properties and the  
16 activity/selectivity towards CH<sub>4</sub> production was also established. Thus, the catalytic  
17 performance can be effectively steered by manipulating the support susceptibility towards  
18 SMSI phenomena.

## 19 **2. EXPERIMENTAL SECTION**

### 20 **2.1 Materials.**

1 The gas cylinders (Ar, 60% H<sub>2</sub>/Ar, 60%H<sub>2</sub>/15%CO<sub>2</sub>/N<sub>2</sub>, 1%CO/Ar, 0.05%CO/Ar,  
2 10%CO<sub>2</sub>/Ar) were purchased from Air Liquid. Chemical reagents, including ceria nitrate  
3 hexahydrate (Ce(NO<sub>3</sub>)<sub>3</sub> •6H<sub>2</sub>O, 99%), Hexamethylenetetramine ((CH<sub>2</sub>)<sub>6</sub>N<sub>4</sub>, HMT, >99%),  
4 oleylamine (OAm, >70%), oleic acid (OA, 90%), nickel(II) acetylacetonate  
5 (Ni(acac)<sub>2</sub>, >95%), borane tributylamine complex (BTB, >95%), Sodium hydroxide  
6 (NaOH, >98%) and SiC were purchased from Sigma Aldrich.

## 7 **2.2 Catalyst Preparation**

8 **Synthesis of Ni Nanoparticles.** The synthesis is a scaled-up process operated on  
9 Schlenk line based on a previously reported procedure [23]. Briefly, in a 100 ml reaction  
10 flask under Ar flow, 514 mg of Ni(acac)<sub>2</sub> (1 mmol) was mixed with 30 mL OAm and 0.64  
11 mL of 1 mmol OA and thoroughly stirred at 110 °C for 20 min. The solution was kept at  
12 110 °C for an hour and evacuated using a vacuum pump 3 times to remove humidity and  
13 oxygen. The solution was subsequently cooled down to 90 °C where 528 mg of BTB  
14 dissolved in 4 mL of OAm quickly injected into the solution. The color change from  
15 green to dark brown could be observed. The resultant solution was maintained at 90 °C  
16 for 60 min before cooled down to room temperature. The product was washed by ethanol  
17 and separated by centrifugation (10000 rpm for 10 min). The resulting Ni particles were  
18 dispersed in hexane for further use.

19 **Synthesis of CeO<sub>2</sub> Nanocrystals.** The synthesis procedure of CeO<sub>2</sub> nanorod

1 (CeO<sub>2</sub>-NR) and nanocube (CeO<sub>2</sub>-NC) were similar as previous literature [24]. These two  
2 morphologies of CeO<sub>2</sub> support were synthesized by hydrothermal method. First, 30 ml of  
3 14 M NaOH solution was added into 40 ml of 0.113M Ce(NO<sub>3</sub>)<sub>3</sub> • 6H<sub>2</sub>O solution under  
4 vigorous stirring. The suspension was stirred for additional 30 min and sealed into a  
5 Teflon-lined stainless-steel autoclave. The suspension was aged in autoclaves for 24 h at  
6 100 and 180 °C to prepare CeO<sub>2</sub>-NR and CeO<sub>2</sub>-NC samples, respectively. The obtained  
7 solid were centrifuged at 8000 rpm for 10 min and thoroughly washed with deionized  
8 water until pH measurement is close to 7. The obtained solids were dried in an oven at  
9 90 °C overnight.

10 For the synthesis of CeO<sub>2</sub> nanooctahedra, a 200 mL reaction flask was filled with 20  
11 mL of 0.0375 M Ce(NO<sub>3</sub>)<sub>3</sub>, 4 mL of 0.5 M hexamethylenetetramine (HMT), and an  
12 additional 20 mL of deionized water. The mixture was stirred at 800 rpm in air for 10 min  
13 and then heated to 75°C and kept for 3 h. The solution slowly turned from clear to milk  
14 white. All synthesized CeO<sub>2</sub> nanocrystals (nanorod, nanocube, nanooctahedra) were  
15 calcined in static air at 400 °C with ramping rate of 1 °C/min for 2 h to remove the  
16 surfactant and obtain the fully oxidized state.

17 **Synthesis of Ni/CeO<sub>2</sub> Catalysts.** The Ni/CeO<sub>2</sub> catalysts were prepared by directly  
18 depositing the as-synthesized Ni NPs solution on to the CeO<sub>2</sub> nanocrystals [25]. Briefly,  
19 the CeO<sub>2</sub> nanocrystals were dispersed in ethanol under sonication, desired amount of Ni  
20 NPs solution was added to the CeO<sub>2</sub>/ethanol mixture dropwise. The resulting mixture was

1 further sonicated for another 30 min. Afterwards, organic solvents were removed with a  
2 rotary evaporator. The obtained solid was dried in an oven at 90 °C overnight and then  
3 calcined in static air at 400 °C for 2 h. The target loading was 1.5wt% for each sample,  
4 which was further verified with ICP-AES analysis.

### 5 **2.3 Catalytic Evaluation**

6 **Steady State CO<sub>2</sub> Hydrogenation Evaluation.** The activity tests of steady-state  
7 CO<sub>2</sub> hydrogenation were performed in a fixed-bed plug flow reactor at atmospheric  
8 pressure. 2.5 mg of catalyst was diluted with 22.5 mg of SiC, sieved into 40-60 mesh,  
9 held in place with quartz wool and loaded into a U-type quartz tube, which yields a  
10 WHSV of 1200 L\*gcat<sup>-1</sup>\*hr<sup>-1</sup> with flow of 60%H<sub>2</sub>/15%CO<sub>2</sub>/N<sub>2</sub> at 50 sccm. Prior to the  
11 reaction test, the catalysts were activated in 10%H<sub>2</sub>/Ar at 50 sccm and 500 °C for 2 h.  
12 The reaction products were analyzed by an online gas chromatography (Ruimin GC 2060,  
13 Shanghai) equipped with a 5A Molecular sieve, Porapak T column, TCD, FID, and a  
14 methanizer. The rates of forward CO and CH<sub>4</sub> formation ( $r_{f,CO}$  and  $r_{f,CH_4}$ ) are obtained  
15 from GC measurements described as equations below.

$$16 \quad r_{f,CO} = F * C_{CO}$$

$$17 \quad r_{f,CH_4} = F * C_{CH_4}$$

18 where F is the flow rate of effluent stream (mol/s), C is the concentration of products  
19 (%) calculated from GC peak area × response factor (%/area). The response factors of

1 CO<sub>2</sub>, CO and CH<sub>4</sub> was calibrated with standard curve methods.

2 The reported net rates ( $r_{n, CO}$  and  $r_{n, CH_4}$ ) were corrected for the approach to  
3 equilibrium for CO<sub>2</sub> methanation and RWGS reactions in order to obtain rigorous net  
4 reaction rates, the equations are demonstrated as follows:

$$5 \quad r_{n,CO} = r_{f,CO} * (1 - \eta_{CO})$$

$$6 \quad r_{n,CH_4} = r_{f,CH_4} * (1 - \eta_{CH_4})$$

7 The approach to equilibrium ( $\eta$ ) are defined as follows:

$$8 \quad \eta_{CO} = \frac{[P_{CO}][P_{H_2O}]}{[P_{CO_2}][P_{H_2}]} \frac{1}{K_{eq,CO}}$$

$$9 \quad \eta_{CH_4} = \frac{[P_{CH_4}][P_{H_2O}]^2}{[P_{CO_2}][P_{H_2}]^4} \frac{1}{K_{eq,CH_4}}$$

10 where  $P_i$  is the partial pressure of the corresponding species. The equilibrium  
11 constants for CO<sub>2</sub> methanation and RWGS reactions at 400 °C were calculated with Van't  
12 Hoff equation to be  $6.48 \times 10^8$  and 0.048, respectively:

$$13 \quad \ln K_{eq} = -\frac{\Delta H^0}{RT} + \frac{\Delta S^0}{R}$$

14 Values of  $\eta_{CO}$  range from 0 to 0.2 for experimental data reported,  $\eta_{CH_4}$  are negligible  
15 values. Since only CO and CH<sub>4</sub> were produced with observable amounts, the rate of CO<sub>2</sub>  
16 conversion (mol/s) is calculated with elemental balance:

1 
$$r_{n,CO_2} = r_{n,CO} + r_{n,CH_4}$$

2 
$$TOF \text{ of } CO_2 \text{ conversion}(s^{-1}) = \frac{r_{n,CO_2} * N_A}{N_{Ni \text{ site}}}$$

3 where  $N_A$  is Avogadro constant and  $N_{Ni \text{ site}}$  is the number of active sites quantified by  
4 CO - Temperature Programmed Reduction (CO-TPR). In CO-TPR, surface Ni-OH and  
5 Ni-O species are reduced by CO according to the following equations, respectively:  $2CO$   
6  $+ 2Ni-OH \rightarrow 2CO_2 + H_2$  and  $CO + NiO \rightarrow CO_2$ . Thus, the number of surface Ni sites can  
7 be quantified by the amount of  $CO_2$  formation (Table S6).

8  $CH_4$  selectivity ( $S_{CH_4}$ ) is calculated by:

9 
$$S_{CH_4} = \frac{r_{n,CH_4}}{r_{n,CO} + r_{n,CH_4}}$$

10 We adopted Koros and Nowak (KN) criterion to examine if the reported activities  
11 are within kinetic regime. The loading of Ni/CeO<sub>2</sub> catalysts were adjusted to vary number  
12 of active sites with WHSV of 2400, 1800, 600 and 240 L\* $g_{cat}^{-1}$ \*hr<sup>-1</sup> at constant reactant  
13 flow of 50 sccm.

14 **Hysteresis Reactivity Test.** To examine if the H<sub>2</sub> activation and reaction induced  
15 SMSI persists after air exposure, the hysteresis reactivity test was performed. NiCe-NO  
16 catalyst is first activated with 10%H<sub>2</sub>/Ar at 500 °C for 2 h followed by CO<sub>2</sub>  
17 hydrogenation reaction at 400 °C for 2 h. The WHSV was adjusted at 600 L\* $g_{cat}^{-1}$ \*hr<sup>-1</sup>.  
18 The NiCe-NO sample is then cooled to room temperature and exposed to air for 12 h,

1 followed by re-examination of CO<sub>2</sub> hydrogenation activity at 400 °C for 2 h. The reaction  
2 procedure is monitored by a Shanghai Linglu mass spectrometer.

### 3 **2.4 Catalyst Characterizations**

4 **TEM Characterization.** The catalyst morphology and particle size information of  
5 Ni/CeO<sub>2</sub> and Ni/SiO<sub>2</sub> catalysts were analyzed by high-resolution transmission electron  
6 microscope (HRTEM) experiments and EDS mapping on a FEI Tecnai G2 F20 electron  
7 microscope equipped with an Oxford spectrometer. The operating accelerating voltage  
8 was 200 kV. The samples were suspended in ethanol using ultrasonication and placed  
9 onto a carbon film supported over a Cu grid.

10 **CO - TPR.** CO-TPR of Ni/CeO<sub>2</sub> samples after CO<sub>2</sub> hydrogenation reaction  
11 treatment were performed on a TP-5080B chemisorption instrument (Tianjin Xianquan  
12 Company), the time-on effluent stream was analyzed by a mass spectrometer (Shanghai  
13 Linglu Company). Typically, 12.5 mg of Ni/CeO<sub>2</sub> catalyst was loaded in each  
14 measurement. After activation with 10%H<sub>2</sub>/Ar at 50 sccm and 500 °C for 2 h and CO<sub>2</sub>  
15 hydrogenation at 400 °C with 60%H<sub>2</sub>/15%CO<sub>2</sub>/N<sub>2</sub> at 50 sccm for 2 h, the catalyst is  
16 flushed with Ar at 400 °C for 15 min to remove any adsorbed reactant or product then  
17 cool to room temperature. CO-TPR experiment was operated from 28 °C to 850 °C with  
18 a ramping rate of 10 °C /min and flow of 1%CO/Ar at 50 sccm. The calibration of CO<sub>2</sub>  
19 formation was performed by flowing 1%CO<sub>2</sub>/Ar (diluted from 10%CO<sub>2</sub>/Ar) at constant

1 flow of 50 sccm.

2 **Quasi *In Situ* XPS Analysis.** Quasi *in situ* X-ray Photoelectron Spectroscopy (XPS)  
3 analysis were performed with a Thermo ESCALAB 250Xi spectrometer equipped with a  
4 monochromatic Al K $\alpha$  radiation source (1486.6 eV, pass energy 20.0 eV). A pretreatment  
5 chamber was used for catalyst activation. Afterwards, the chamber was evacuated, and  
6 the sample was directly transferred into the analysis chamber in vacuum to avoid  
7 exposure to air. The spectra for H<sub>2</sub> activated catalysts were collected by pretreating the  
8 samples in 10%H<sub>2</sub>/Ar at 500 °C for 2 h. The spectra for H<sub>2</sub> activated + reaction treated  
9 catalysts were collected by treating the samples in 10%H<sub>2</sub>/Ar at 500 °C for 2 h followed  
10 by 60%H<sub>2</sub>/15%CO<sub>2</sub>/N<sub>2</sub> at 400 °C for 2 h.

11 ***In Situ* DRIFTS.** The *in situ* diffuse reflectance infrared Fourier transform spectra  
12 (DRIFTS) during CO<sub>2</sub> hydrogenation and the subsequent room temperature adsorption of  
13 CO were measured on a Nicolet Model iS-50 FT-IR spectrometer equipped with an  
14 MCT/A detector. 2.5 mg of each catalyst sample was supported on quartz wool and  
15 placed in reactor cell. The steady state *in situ* DRIFTS spectra were collected with  
16 60%H<sub>2</sub>/15%CO<sub>2</sub>/N<sub>2</sub> at 400 °C from 1 to 60 min with flow of 50 sccm after pretreating  
17 the catalysts in 10% H<sub>2</sub> at 500 °C for 2 h. The temperature dependent *in situ* DRIFTS  
18 spectra were collected with 60%H<sub>2</sub>/15%CO<sub>2</sub>/N<sub>2</sub> from 150 to 400 °C with flow of 50  
19 sccm after pretreating the catalysts in 10% H<sub>2</sub> at 500 °C for 2 h and cooled down to  
20 150 °C in 10% H<sub>2</sub>.

1            *In situ* DRIFTS of room temperature CO adsorption was performed after treating the  
2 catalyst with H<sub>2</sub> activation and reaction conditions for 2 h then cooling down to room  
3 temperature in Ar flow. The CO was first adsorbed by flowing 50 sccm of 0.05% CO/Ar  
4 (Air Liquid) at room temperature for 30 min to allow adsorption saturation, then spectra  
5 were collected. A configuration of our *in situ* DRIFTS cell is demonstrated in Figure S10.  
6 The temperature ramping rate of the *in situ* DRIFTS measurements (room temperature to  
7 500 °C during activation and 150 to 400 °C during reaction) was controlled at ~  
8 20 °C/min and spectra of in situ spectra of CO<sub>2</sub> hydrogenation were taken every 50 °C  
9 increment.

10            ***In Situ FT-IR.*** *In situ* Fourier-transform infrared spectroscopy (FT-IR) of CO  
11 adsorption at liquid-nitrogen temperature were conducted using a BRUKER TENSOR 27  
12 spectrometer equipped with an *in situ* reaction cell. About 10 mg of the NiCe-NR,  
13 NiCe-NC and NiCe-NO catalyst was pressed into a pellet. The catalyst was exposed to  
14 aforesaid hydrogen activation and CO<sub>2</sub> hydrogenation reaction condition in the IR cell,  
15 cooled under vacuum to *ca.* -150 °C, and subsequently CO was continuously pulsed into  
16 the cell. The measurements were carried out in transmission mode with a resolution of 4  
17 cm<sup>-1</sup> and accumulations of 256 scans. A spectrum of the empty cell at *ca.* -150 °C was  
18 taken as a background for the measurements.

19            ***In Situ Raman Spectroscopy.*** The *in situ* Raman spectra were collected with a  
20 Horiba LabRam-HR spectrometer equipped with a visible laser excitation at 514 nm

1 generated by a He-Cd laser. The laser was focused on the sample with a confocal  
2 microscope equipped with a 50X long working distance objective (Olympus  
3 BX-30-LWD), and the scattered photons were directed and focused onto a single-stage  
4 monochromator and measured with a UV-sensitive LN2-cooled CCD detector (Horiba  
5 CCD-3000 V). The collection range was from 100 to 1800  $\text{cm}^{-1}$ . The spectra for  $\text{H}_2$   
6 activated sample was collected in 10%  $\text{H}_2$  atmosphere after pretreating the catalyst in  
7 10% $\text{H}_2$ /Ar at 500 °C for 2 h. The spectra  $\text{H}_2$  activated + reaction treated catalysts were  
8 collected in reactant stream by treating the samples in 10% $\text{H}_2$ /Ar at 500 °C for 2 h  
9 followed by 60% $\text{H}_2$ /15% $\text{CO}_2$ / $\text{N}_2$  at 400 °C for 2 h. The temperature ramping rate is  
10 controlled at ~20 °C /min for all heating processes.

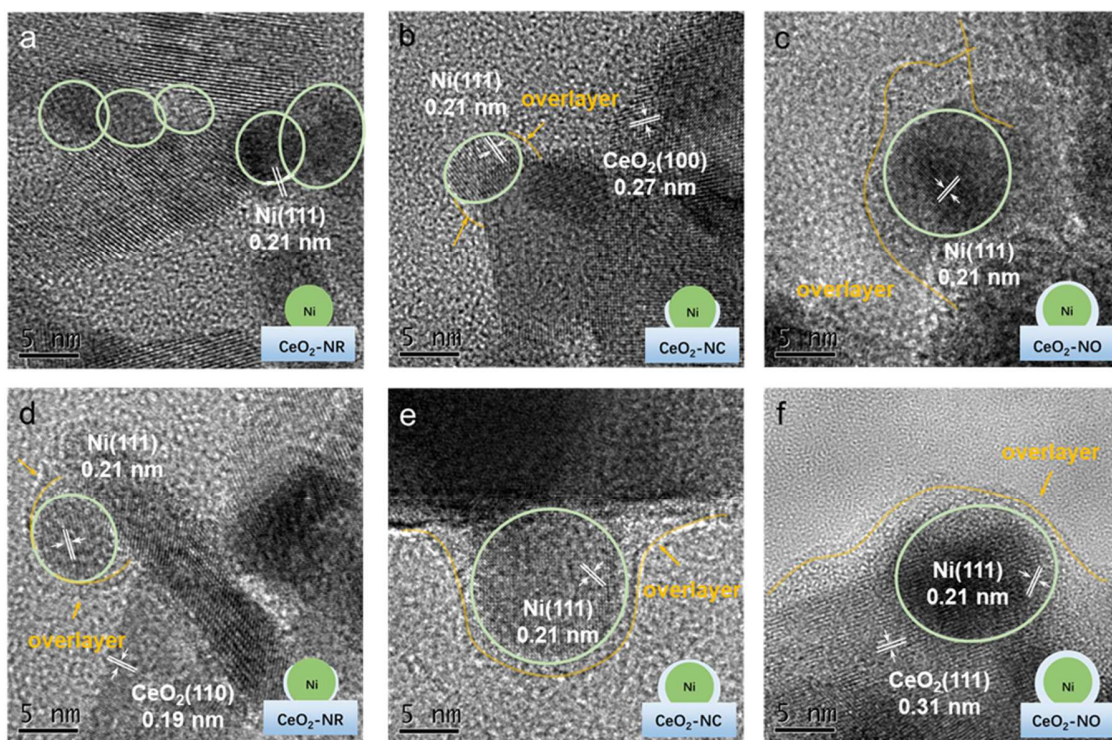
### 11 **3. RESULTS AND DISCUSSIONS**

#### 12 **3.1 Morphologies of Catalysts**

13 Three types of  $\text{CeO}_2$  supports were synthesized: nanorod with exposed (110) and  
14 (100) facets, nanocube with a (100) facet and nanooctahedra with a (111) facet (Figure S1)  
15 [23]. It has been previously reported that Ni particles with various particle size (2 nm – 8  
16 nm) supported on  $\text{CeO}_2$  possess distinct catalytic performance. The Ni/ $\text{CeO}_2$  catalyst with  
17 Ni NPs ~ 8 nm demonstrates superior activity and  $\text{CH}_4$  selectivity than the 2 nm and 4  
18 nm counterparts due to the enhanced ability of hydrogenating formate intermediate [26].  
19 Thus, to avoid the large variation in Ni particle size resulted from traditional wet  
20 impregnation method, we first synthesized monodispersed NPs with an average size of *ca.*  
21 3.5 nm and uniform dispersion using a colloidal synthesis method (Figure S2), followed

1 by direct deposition of Ni NPs onto different CeO<sub>2</sub> nanocrystals with a Ni loading of ~1.5  
2 wt.% [24]. The resulting supported Ni catalysts are denoted as NiCe-NR, NiCe-NC and  
3 NiCe-NO, respectively. High-angle annular dark-field - scanning transmission electron  
4 microscopy (HAADF-STEM) images with elemental mapping show that all three  
5 samples exhibit dispersed partially oxidized Ni NPs with average particle size of ~5 nm  
6 after the calcination treatment (Figure S3, Table S5).

7 The high resolution (HR) TEM images of NiCe samples reveal that the supported  
8 NiCe-NR catalyst possesses almost a clean Ni surface after reduction by 10%H<sub>2</sub> at  
9 500 °C for 2 h, while overlayers are present for the supported NiCe-NC (< 1 nm layer,  
10 not fully encapsulated) and NiCe-NO (1-2 nm layer, fully encapsulated) catalysts  
11 (Figures 1a-c). Exposure of the catalysts to the CO<sub>2</sub> hydrogenation reaction environment  
12 (60%H<sub>2</sub>/15%CO<sub>2</sub>, 400 °C) for 2 h results in more significant encapsulation of the Ni NPs  
13 (Figures 1d-f). The overlayer is likely to be amorphous CeO<sub>x</sub> species owing to the SMSI  
14 effect since *in situ* Raman analysis rule out carbon deposition (absence of characteristic  
15 bands at *ca.* 1600 and 1320 cm<sup>-1</sup>) (Figure S4) [27]. A conclusion can be drawn that the  
16 CO<sub>2</sub> methanation reaction induces a more pronounced SMSI phenomenon between the Ni  
17 NPs (4-9 nm) and CeO<sub>2</sub> support than the 10%H<sub>2</sub> reduction treatment, with the extent of  
18 the overlayer following the order of NiCe-NO > NiCe-NC > NiCe-NR [28]. The schemes  
19 of each catalyst after different treatments are provided as insets in Figure 1. The  
20 supported Ni particles are stable and only slightly grow in size after the reduction and  
21 reaction treatments (Table S5).



1  
 2 **Figure 1.** Representative high resolution TEM images and schematic illustration of the  
 3 SMSI effect in (a) Ni/CeO<sub>2</sub>-nanorod (NiCe-NR), (b) Ni/CeO<sub>2</sub>-nanocube (NiCe-NC) and  
 4 (c) Ni/CeO<sub>2</sub>-nanooctahedra (NiCe-NO) after H<sub>2</sub> activation treatment (10%H<sub>2</sub> at 500 °C  
 5 for 2 h) and (d) NiCe-NR, (e) NiCe-NC and (f) NiCe-NO after H<sub>2</sub> activation and CO<sub>2</sub>  
 6 methanation reaction at 400 °C for 2 h.

### 7 **3.2 Catalytic Performance**

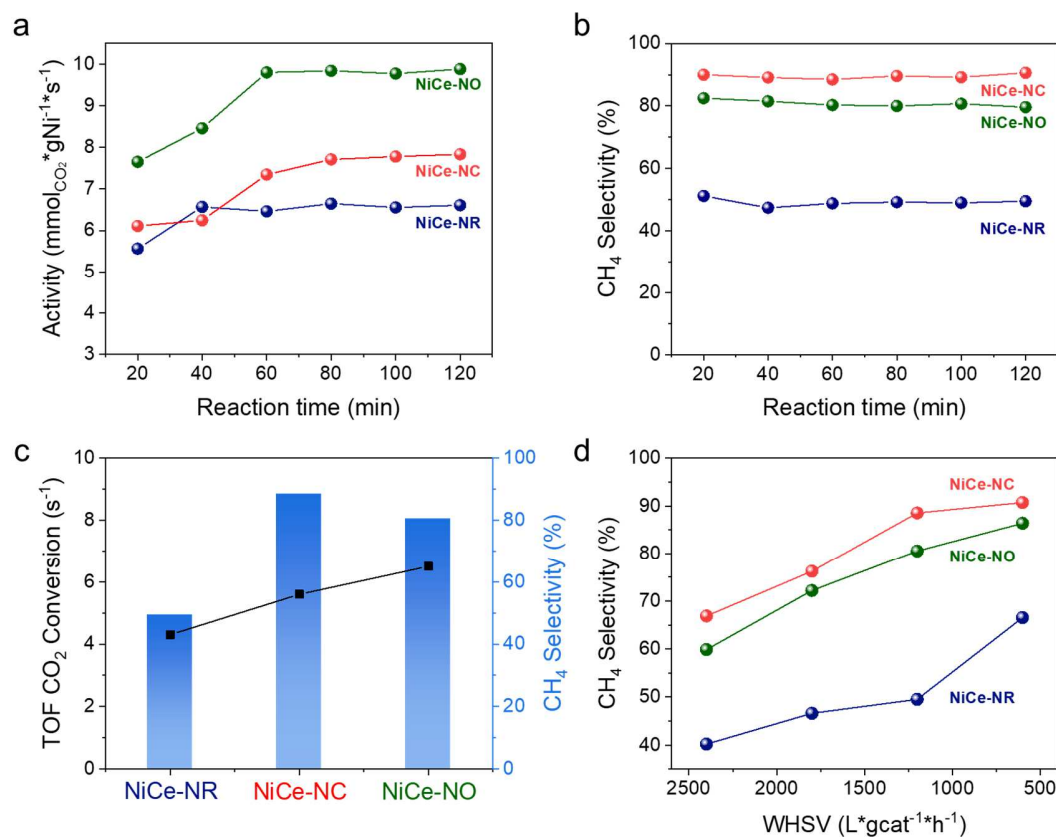
8 We first demonstrate the examination of the influence of heat and mass transport on  
 9 the reaction condition in supplementary material. The intraparticle mass transport was  
 10 evaluated with Weisz-Prater criterion, intraparticle heat transport was examined under  
 11 Anderson criterion while external heat and mass transport was checked with Mears's  
 12 criterion [29,30]. Furthermore, under the examination of KN criterion, the reported rates

1 in Figure 2 are within kinetic regime. Thus, the measured rates of CO and CH<sub>4</sub> formation  
2 do reflect the intrinsic reactivities of Ni/CeO<sub>2</sub> catalysts.

3 Catalytic reaction of CO<sub>2</sub> hydrogenation over Ni-based catalysts at 1 atm generally  
4 involves CO<sub>2</sub> methanation ( $\text{CO}_2 + 4\text{H}_2 \rightarrow \text{CH}_4 + 2\text{H}_2\text{O}$ ,  $\Delta H_{298\text{K}} = -165 \text{ kJ/mol}$ ) as well as  
5 RWGS reaction ( $\text{CO}_2 + \text{H}_2 \rightarrow \text{CO} + \text{H}_2\text{O}$ ,  $\Delta H_{298\text{K}} = 41.2 \text{ kJ/mol}$ ). According to numerical  
6 solutions from literature [31,32], CO<sub>2</sub> hydrogenation to CH<sub>4</sub> is highly exothermic and  
7 thermodynamically favored at  $T < 800\text{-}900 \text{ K}$ . At higher temperature, the reaction  
8 becomes more selective to CO. Thus, more endothermic and thermodynamically limited.  
9 In the present work, to study the reaction induced SMSI effect and examine the WHSV  
10 dependent product selectivity, the steady state performance of the supported Ni catalysts  
11 for the CO<sub>2</sub> methanation reaction was evaluated at 400 °C and low conversions (< 15%),  
12 thus free from the thermodynamic constrains.

13 As shown in Figure 2a, the supported NiCe-NC and NiCe-NO catalysts exhibit a  
14 continuous increase of activity in the first hour of reaction after H<sub>2</sub> reduction while the  
15 activity remains almost unchanged for the supported NiCe-NR catalyst. The trend of  
16 activities coincides well with the aforesaid dynamics of CeO<sub>x</sub> overlayers upon reaction  
17 treatment. The CH<sub>4</sub> selectivity, on the other hand, did not exhibit significant variation as  
18 the reaction proceeds (Figure 2b). We adopted CO-TPR as the primary method for  
19 quantification of active sites on Ni/CeO<sub>2</sub> catalysts [33,34]. The CO<sub>2</sub> formation spectra are  
20 demonstrated in Figure S5, detailed procedures of calculation are provided in  
21 supplementary material. Figure 2c indicates that NiCe-NO and NiCe-NC which show

1 higher degree of SMSI effect, possess higher turn-over frequency (TOF) of CO<sub>2</sub>  
2 (NiCe-NO: 6.5 s<sup>-1</sup>; NiCe-NC: 5.6 s<sup>-1</sup>) than NiCe-NR (4.3 s<sup>-1</sup>). As exhibited in Figure S6,  
3 we examine the reported reaction rates with Koros and Nowak (KN) criterion. The slopes  
4 of [rate of CO<sub>2</sub> conversion (mol/s<sup>-1</sup>g<sub>cat</sub><sup>-1</sup>)] vs [surface moles of Ni site per unit weight of  
5 catalyst] is constant for all catalysts with weight hourly space velocity (WHSV) ranges  
6 from 2400 to 600 L·gcat<sup>-1</sup>·hr<sup>-1</sup>, which indicates the reported CO<sub>2</sub> conversion activities in  
7 Figure 2 are linearly proportional to surface active sites thus under kinetic regime [35].  
8 Furthermore, the selectivities of CO<sub>2</sub> methanation show a strong dependence on the  
9 WHSV as illustrated in Figure 2d. With the WHSV decrease from 2400 to 600  
10 L·gcat<sup>-1</sup>·hr<sup>-1</sup>, CH<sub>4</sub> selectivity dramatically increased from 66.9% to 90.7% over NiCe-NC,  
11 59.9% to 86.4% over NiCe-NO and 40.2% to 66.5% over NiCe-NR. The  
12 WHSV-sensitivity of CH<sub>4</sub> selectivity suggests that CO<sub>ads</sub> is a key intermediate for the  
13 consecutive CO methanation to CH<sub>4</sub> [36,37]. The drastic difference in CH<sub>4</sub> selectivity  
14 suggests different degrees of participation of CO<sub>2</sub> activation and the CO<sub>ads</sub>-pathway in  
15 CO<sub>2</sub> methanation, which depends on the structures of Ni/CeO<sub>2</sub> catalyst. It is noticed that  
16 in the *ex situ* HRTEM images (Figure 1 d-f), the encapsulation layers are observed after  
17 the samples were transferred from steady state reactor to TEM instrument and exposed to  
18 air. Thus, we performed hysteresis activity test on NiCe-NO which exhibited the highest  
19 activity (Figure S7) to examine if the SMSI state can be preserved. The same CO<sub>2</sub>  
20 hydrogenation activity is recovered upon running the reaction twice after air exposure  
21 overnight, which suggests the SMSI between Ni and CeO<sub>2</sub> is stable. The initial induction



1 procedure might be bypassed when catalyst is reused after room temperature air exposure  
 2 for short periods of time.

3 **Figure 2.** (a) Time dependent CO<sub>2</sub> hydrogenation activity of Ni/CeO<sub>2</sub> catalysts during the  
 4 first 120 minutes of reaction at 400 °C with WHSV of 1200 L\*gc<sup>-1</sup>\*hr<sup>-1</sup>, (b) Time  
 5 dependent CH<sub>4</sub> selectivity of CO<sub>2</sub> hydrogenation of Ni/CeO<sub>2</sub> catalysts during the first 120  
 6 minutes of reaction with WHSV of 1200 L\*gc<sup>-1</sup>\*hr<sup>-1</sup>, (c) Steady state CO<sub>2</sub>  
 7 hydrogenation performance of Ni/CeO<sub>2</sub> catalysts at WHSV of 1200 L\*gc<sup>-1</sup>\*hr<sup>-1</sup>, (d)  
 8 Dependency of CH<sub>4</sub> selectivity on WHSV over Ni/CeO<sub>2</sub> catalysts.

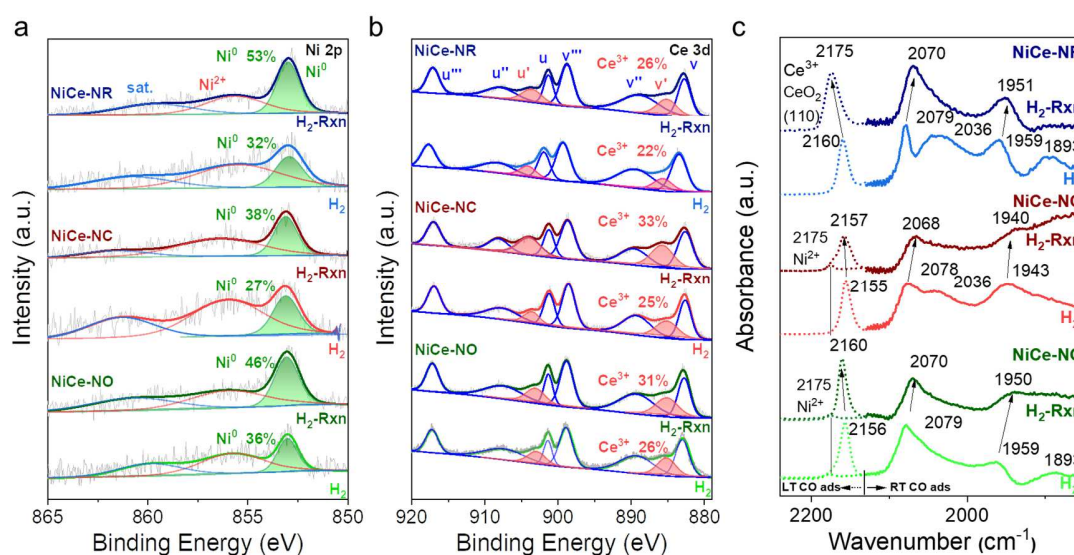
### 9 3.3 Detailed Structures of Ni/CeO<sub>2</sub> Catalysts

1 First, quasi *in situ* XPS analysis was performed to establish correlations between  
2 structural changes and catalytic performance. Exposure of the catalyst to both hydrogen  
3 and the reaction atmosphere results in reduction of the initially oxidized Ni NPs, with the  
4 percentage of Ni<sup>0</sup> determined to be 27-36% (H<sub>2</sub> reduced) and 38-53% (H<sub>2</sub> reduced and  
5 then reaction treated), respectively (Figure 3a). The reason why ceria supported Ni is not  
6 fully reduced from Ni<sup>2+</sup> could be ascribed to the formation of NiO-CeO<sub>x</sub> solid solution or  
7 the electronic metal-support interaction (EMSI) at the interfaces of Ni NPs and CeO<sub>2</sub>  
8 support [16,18,38]. Furthermore, encapsulation of Ni NPs by the CeO<sub>x</sub> overlayer due to  
9 the SMSI effect should, in theory, further strengthen such an EMSI effect [16,18]. The  
10 degree of reduction of CeO<sub>2</sub> is also enhanced as evidenced by the increased presence of  
11 the Ce<sup>3+</sup> species (884.8 and 903.7 eV) and oxygen vacancy (O<sub>v</sub>) sites (531.7-532.0 eV)  
12 (Figure 3b, Figure S8) [39]. The percentages of Ce<sup>3+</sup> and O<sub>v</sub> for catalysts after H<sub>2</sub>  
13 activation and reaction treatment are summarized in Table S7, which follow the same  
14 trend of NiCe-NC ≈ NiCe-NO > NiCe-NR. It is noted that formation of oxygen defects in  
15 CeO<sub>2</sub> has been considered as a prerequisite for its migration on metallic Ni NPs [16,18].  
16 Combining the XPS and TEM results, it seems that the extent of SMSI increases with  
17 more reduced supports [40]. It is worth mentioning that despite the majority of literature  
18 reports a superior catalytic performance on active metals supported on CeO<sub>2</sub>-NR over  
19 other morphologies [24,41,42], a number of studies reveal that CeO<sub>2</sub>-NC and CeO<sub>2</sub>-NO  
20 also demonstrated enhanced reducibility and catalytic performance, especially under  
21 strong reducing reaction environment, which is in agreement with the present work [43–

1 45].

2 We further performed *in situ* FT-IR analysis using CO as the probe molecule to gain  
3 a complete insight into the nickel surface. The low temperature measurement was  
4 undertaken at -150 °C in transmission mode to probe CO adsorption on Ni<sup>2+</sup> and CeO<sub>x</sub>  
5 species and at room temperature in a diffuse reflectance mode to probe the metallic Ni  
6 sites. Low-temperature CO-IR shows CO<sub>ads</sub> bands on CeO<sub>2</sub> that blueshifts from 2160 to  
7 2175 cm<sup>-1</sup> for NiCe-NR, 2155 to 2157 cm<sup>-1</sup> for NiCe-NC and 2156 to 2160 for NiCe-NO  
8 after reaction, providing another evidence for the reduction of CeO<sub>2</sub> component during  
9 the CO<sub>2</sub> methanation reaction (Figure 3c) [39]. Meanwhile, previous literature suggest IR  
10 bands at 2198, 2184, 2173 and 2162 cm<sup>-1</sup> should be assigned to CO adsorption on Ni<sup>2+</sup>  
11 species [46]. A 2175 cm<sup>-1</sup> band could be deconvoluted which is associated CO adsorption  
12 on Ni<sup>2+</sup> and only appears on the catalyst under significant SMSI (NiCe-NO-H<sub>2</sub>,  
13 NiCe-NO-Rxn and NiCe-NC-Rxn). On NiCe-NR, the Ni<sup>2+</sup>-CO adsorption band is  
14 overlapped with defective CeO<sub>2</sub> (110)-CO which also appears at 2175 cm<sup>-1</sup> thus hard to  
15 be distinguished [39]. As demonstrated in the room temperature CO-DRIFTS spectra,  
16 over the H<sub>2</sub> activated Ni/CeO<sub>2</sub> catalysts, carbonyls (2078 cm<sup>-1</sup>), linear CO adsorption  
17 (2036 cm<sup>-1</sup>) as well as bridged CO adsorption (1959, 1943, 1893 cm<sup>-1</sup>) were found on Ni<sup>0</sup>  
18 [47,48]. After CO<sub>2</sub> hydrogenation, a new band at 2070 cm<sup>-1</sup> (CO on encapsulated  
19 metal-support interfacial region) [49,50] is formed through the merge of 2079 and 2036  
20 cm<sup>-1</sup> band, provide strong piece of evidence for encapsulation of the Ni NPs. Bridged CO  
21 adsorption peaks also experienced redshift (1959 to 1951 cm<sup>-1</sup> over NiCe-NR, NiCe-NO

1 and 1943 to 1940  $\text{cm}^{-1}$  over NiCe-NC), suggesting significant changes on surface  
 2 electronic status. The CO-DRIFTS spectra demonstrate excellent agreements with the  
 3 degree of SMSI effect of the three catalysts observed in HRTEM images. NiCe-NO  
 4 readily possess the interfacial CO adsorption band at 2070  $\text{cm}^{-1}$  upon  $\text{H}_2$  treatment,  
 5 meanwhile, NiCe-NC and NiCe-NR exhibit merging of 2079  $\text{cm}^{-1}$  and 2030  $\text{cm}^{-1}$  peaks  
 6 into 2070  $\text{cm}^{-1}$  band only after SMSI effect induced from extensive reaction treatments.  
 7 In addition, NiCe-NR which exhibits partial encapsulation as evidenced by HRTEM  
 8 image in Figure 1d still possess a strong 1951  $\text{cm}^{-1}$  band that correspond to bridged CO  
 9 adsorption on  $\text{Ni}^0$ , which suggests a significant portion of metallic Ni is exposed and not  
 10 well capsulated by  $\text{CeO}_x$ . Furthermore, the observed adsorption of CO at Ni sites under  
 11 room temperature also indicates the amorphous  $\text{CeO}_x$  layer induced by the SMSI effect is  
 12 permeable to reactant molecules such as CO.



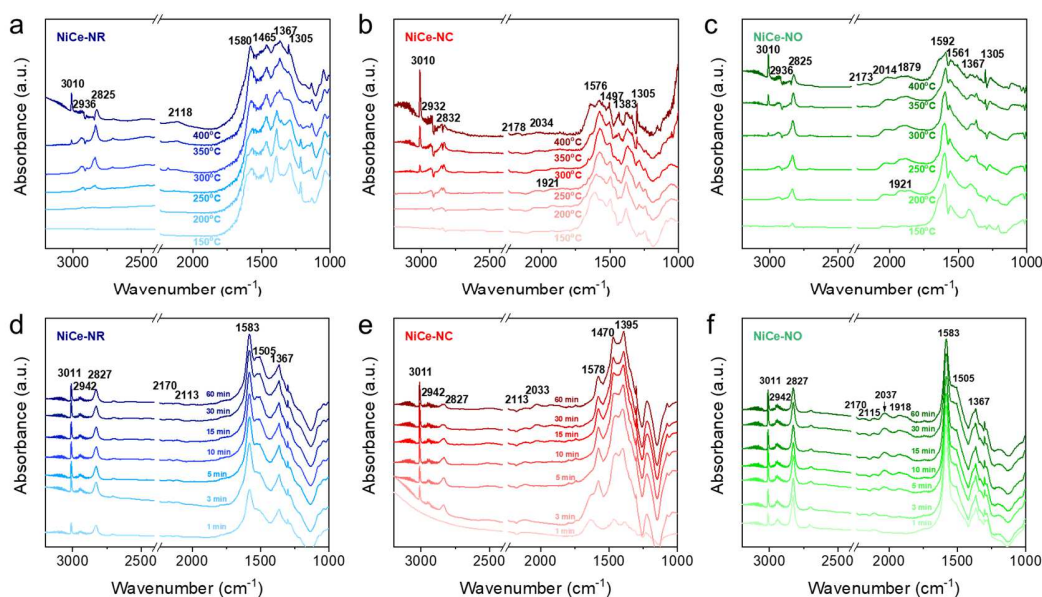
13  
 14 **Figure 3.** (a) Quasi *in situ* Ni 2p XPS spectra of Ni/CeO<sub>2</sub> catalysts. (b) Quasi *in situ* Ce

1 3d XPS spectra of Ni/CeO<sub>2</sub> catalysts and (c) *In situ* FT-IR spectra of low temperature CO  
2 adsorption (left portion) and room temperature DRIFTS of CO adsorption (right portion)  
3 of Ni/CeO<sub>2</sub> catalysts. The treatment procedure follows the same for all spectroscopic  
4 measurements, which involves 10% H<sub>2</sub> activation at 500 °C for 2 h (bottom) and 10% H<sub>2</sub>  
5 activation followed by 2 h of CO<sub>2</sub> hydrogenation reaction at 400 °C (top).

### 6 **3.4 Catalytic Mechanism**

7 With the aid of *in situ* DRIFTS, the variation in CO<sub>2</sub> hydrogenation performance  
8 was correlated with the CO<sub>2</sub> activation pathways over different sites on Ni/CeO<sub>2</sub> catalysts.  
9 Figures 4a-c illustrate the *in situ* temperature dependent DRIFTS of the H<sub>2</sub> activated  
10 Ni/CeO<sub>2</sub> catalysts during CO<sub>2</sub> hydrogenation, respectively. It can be observed that the  
11 3010 cm<sup>-1</sup> peak associated with CH<sub>4</sub> formation appears at *ca.* 300 °C on NiCe-NR and *ca.*  
12 250 °C on NiCe-NC and NiCe-NO (Figure 4a-c), which is in line with the higher activity  
13 observed on NiCe-NC and NiCe-NO catalysts (Figure 2c). Interestingly, both CO<sub>ads</sub>  
14 species (2014-2034, 1918 and 1879 cm<sup>-1</sup>) [47] and surface formate species (HCO<sub>2</sub>, 2942,  
15 2827 and 1583 and 1367 cm<sup>-1</sup>) [4,51–53] appear on supported NiCe-NC and NiCe-NO at  
16 150-200 °C, whereas only surface formate species are detected on supported NiCe-NR  
17 starting from 250 °C. The increased production of CH<sub>4</sub> at higher temperature is in  
18 accordance with the consumption of surface formate and/or CO<sub>ads</sub> species over NiCe-NC  
19 and NiCe-NO (Figure 4b, 4c). Figures 4d-f demonstrated the *in situ* time resolved  
20 DRIFTS of H<sub>2</sub> activated Ni/CeO<sub>2</sub> catalysts under CO<sub>2</sub> hydrogenation at 400 °C. The  
21 evolution trends of reaction intermediates are plotted in Figure S9. It is found that CO<sub>ads</sub>

1 species gradually enriched on NiCe-NC and NiCe-NO (Figure 4e, Figure 4f) while on  
 2 NiCe-NR, CO<sub>ads</sub> species is absent (Figure 4d). Thus, it is likely that CO<sub>2</sub> methanation  
 3 proceeds via different reaction mechanisms over the CeO<sub>x</sub> encapsulated Ni sites  
 4 (NiCe-NC and NiCe-NO) and exposed Ni particles (NiCe-NR).

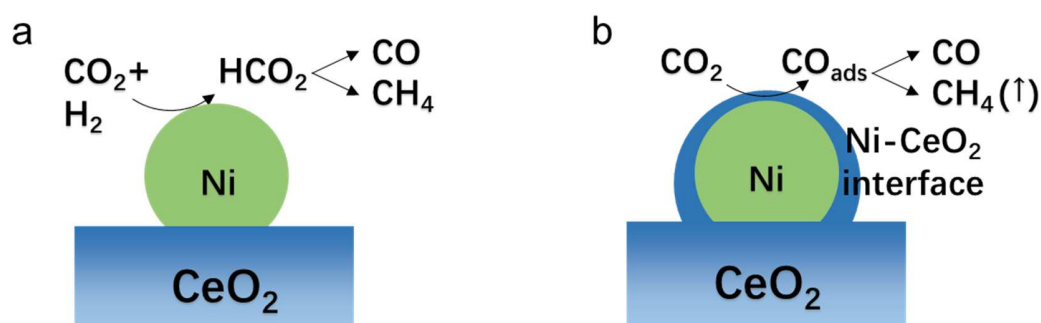


5  
 6 **Figure 4.** *In situ* temperature dependent DRIFTS of a) NiCe-NR, b) NiCe-NC and c)  
 7 NiCe-NO under CO<sub>2</sub> hydrogenation after H<sub>2</sub> activation. Temperature ramping rate:  
 8 20 °C/min. *In situ* time resolved DRIFTS of d) NiCe-NR, e) NiCe-NC and f) NiCe-NO  
 9 under CO<sub>2</sub> hydrogenation at 400 °C after H<sub>2</sub> activation.

10 In general, the CO<sub>2</sub> methanation reaction follows a CO route, with the formation of  
 11 CO<sub>ads</sub> as the key intermediates, or a non-CO route, with HCOO<sub>ads</sub> formed from  
 12 interaction of CO<sub>2</sub> with hydroxyl groups and a hydrogen atom, directly converting to CH<sub>4</sub>.  
 13 For the CO route, the CO<sub>2</sub> activation step, which produces CO<sub>ads</sub>, can proceed via either  
 14 direct dissociation on an oxygen vacancy site (known as the “redox” mechanism) or

1 decomposition of  $\text{HCOO}_{\text{ads}}$  (known as the “associative” mechanism) [13,46,54,55].  
2 According to the literature,  $\text{CO}_2$  activation over Ni particles with 6-9 nm sized particles  
3 mainly follow a CO route with  $\text{CO}_2$  activated through a  $\text{HCOO}_{\text{ads}}$  pathway [37,54,56].  
4 However, oxygen vacancies on reducible supports such as  $\text{CeO}_2$  are capable of activating  
5  $\text{CO}_2$  at low temperatures through the redox mechanism [7,57]. In our case, as  
6 demonstrated by *in situ* DRIFTS, the much lower light-off temperature for  $\text{CO}_{\text{ads}}$  and  $\text{CH}_4$   
7 formation for NiCe-NC and NiCe-NO, with pronounced SMSI phenomenon, suggests  
8 that the redox mechanism possess a much lower barrier, and the rate-determining-step  
9 (RDS) might be the conversion of  $\text{CO}_{\text{ads}}$  to  $\text{CH}_4$ . In contrast, the associative pathway  
10 prevails over the redox pathway over NiCe-NR due to the weak SMSI effect.  
11 Furthermore, given that all three catalysts show similar abilities to adsorb CO molecules  
12 during the CO-DRIFTS measurements, the absence of  $\text{CO}_{\text{ads}}$  species from the *in situ*  
13 temperature dependent DRIFTS spectra for NiCe-NR might suggest that the  
14  $\text{HCOO}$ -to-CO conversion is the RDS. The much lower coverage of  $\text{CO}_{\text{ads}}$  and  $\text{CO}_2$   
15 activation rate for NiCe-NR result in more apparent WHSV dependency and,  
16 consequently, lower  $\text{CH}_4$  selectivity at the high WHSV. The time dependent evolution of  
17 reaction intermediates under  $\text{CO}_2$  hydrogenation in Figure S9b reveals that subtle  
18 changes take place under the reaction induced SMSI effect. The increasing  $\text{CH}_4$   
19 production correlates with the increased  $\text{CO}_{\text{ads}}$  intermediate on NiCe-NC and NiCe-NO,  
20 which shows agreements with the continuous increase in  $\text{CO}_2$  hydrogenation activity  
21 shown in Figure 2a. The corresponding site-sensitive  $\text{CO}_2$  activation through the

1 associative pathway and redox pathway on Ni/CeO<sub>2</sub> catalysts are schematically illustrated  
 2 in Scheme 1a and Scheme 1b, respectively. According to recent DFT investigation [58],  
 3 over Ni/CeO<sub>2</sub> (111) surface, CO<sub>2</sub> methanation through the RWGS + CO-hydrogenation  
 4 (CO pathway) exhibits a lower activation energy barrier (315.18 kJ/mol) over the formate  
 5 route (associative pathway, 428.76 kJ/mol) and direct C–O bond cleavage pathway  
 6 (352.63 kJ/mol). Our study points out under SMSI effect on Ni/CeO<sub>2</sub> catalyst, the RWGS  
 7 + CO-hydrogenation pathway is favored at Ni-CeO<sub>2</sub> interface, which facilitates CH<sub>4</sub>  
 8 production.



9  
 10 **Scheme 1.** (a) Schematic illustration of CO<sub>2</sub> activation with associative mechanism over  
 11 exposed Ni<sup>0</sup> surface and (b) Schematic illustration of CO<sub>2</sub> activation with redox  
 12 mechanism over Ni-CeO<sub>2</sub> interfacial sites.

13

## 14 CONCLUSIONS

15 In conclusion, we demonstrate the Ni nanoparticles on different CeO<sub>2</sub> supports show  
 16 distinct surface structures and catalytic performance in the CO<sub>2</sub> hydrogenation reaction  
 17 due to various susceptibility to SMSI effect. The integration of HRTEM and quasi *in situ*

1 XPS analysis indicates the encapsulation of Ni NPs with amorphous CeO<sub>x</sub> induced by the  
2 SMSI effect during H<sub>2</sub> activation and CO<sub>2</sub> hydrogenation reaction. Ni particles supported  
3 on CeO<sub>2</sub> nanooctahedra and nanocube benefit the most from the SMSI effect. The extent  
4 of encapsulation is closely associated with the capability of forming oxygen vacancies,  
5 which is proved to activate CO<sub>2</sub> at low temperatures. The CO<sub>2</sub> hydrogenation pathway  
6 also depends on the catalyst structure. NiCe-NC and NiCe-NO benefit from the SMSI  
7 phenomenon possess an abundance of interfacial sites that favor redox mechanism with  
8 CO methanation to be the slow step. Meanwhile, the NiCe-NR with a limited SMSI effect  
9 activates CO<sub>2</sub> with slower kinetics and shows lower activity and CH<sub>4</sub> selectivity. Our  
10 findings shed light on the understanding of the structure-activity relationship in CO<sub>2</sub>  
11 hydrogenation and new strategies of improving reaction activity and selectivity through  
12 tuning the support facet-dependent SMSI effect.

13

#### 14 **ACKNOWLEDGMENT**

15 This work is sponsored by the National Key R&D Program of China (2018YFB0604501),  
16 National Natural Science Foundation of China (22078089), Program for Professor of  
17 Special Appointment (Eastern Scholar) at Shanghai Institutions of Higher Learning and  
18 Shanghai Sailing Program (19YF1410600). The research at Lehigh University was  
19 supported by the Center for Understanding & Control of Acid Gas-Induced Evolution of  
20 Materials for Energy (UNCAGE-ME), an Energy Frontier Research Center funded by

1 DOE, Office of Science, Office of Basic Energy Sciences under grant DE-SC0012577.

## 2 REFERENCES

- 3 [1] H. Yang, C. Zhang, P. Gao, H. Wang, X. Li, L. Zhong, W. Wei, Y. Sun, *Catal. Sci.*  
4 *Technol.* 7 (2017) 4580–4598.
- 5 [2] M.-M. Millet, G. Algara-Siller, S. Wrabetz, A. Mazheika, F. Girgsdies, D.  
6 Teschner, F. Seitz, A. Tarasov, S. V. Levchenko, R. Schlögl, E. Frei, *J. Am. Chem.*  
7 *Soc.* 141 (2019) 2451–2461.
- 8 [3] T.S. Galhardo, A.H. Braga, B.H. Arpini, J. Szanyi, R. V. Gonçalves, B.F. Zornio,  
9 C.R. Miranda, L.M. Rossi, *J. Am. Chem. Soc.* 143 (2021) 4268–4280.
- 10 [4] S. Kattel, B. Yan, Y. Yang, J.G. Chen, P. Liu, *J. Am. Chem. Soc.* 138 (2016)  
11 12440–12450.
- 12 [5] T. Cai, H. Sun, J. Qiao, L. Zhu, F. Zhang, J. Zhang, Z. Tang, X. Wei, J. Yang, Q.  
13 Yuan, W. Wang, X. Yang, H. Chu, Q. Wang, C. You, H. Ma, Y. Sun, Y. Li, C. Li,  
14 H. Jiang, Q. Wang, Y. Ma, *Science* 373 (2021) 1523–1527.
- 15 [6] X. Su, X.F. Yang, Y. Huang, B. Liu, T. Zhang, *Acc. Chem. Res.* 52 (2019) 656–  
16 664.
- 17 [7] S. Tada, H. Nagase, N. Fujiwara, R. Kikuchi, *Energy and Fuels* 35 (2021) 5241–  
18 5251.
- 19 [8] C. Vogt, M. Monai, E.B. Sterk, J. Palle, A.E.M. Melcherts, B. Zijlstra, E.  
20 Groeneveld, P.H. Berben, J.M. Boereboom, E.J.M. Hensen, F. Meirer, I.A.W. Filot,  
21 B.M. Weckhuysen, *Nat. Commun.* 10 (2019) 5330.

- 1 [9] C. Vogt, M. Monai, G.J. Kramer, B.M. Weckhuysen, *Nat. Catal.* 2 (2019) 188–  
2 197.
- 3 [10] C. Vogt, E. Groeneveld, G. Kamsma, M. Nachtegaal, L. Lu, C.J. Kiely, P.H.  
4 Berben, F. Meirer, B.M. Weckhuysen, *Nat. Catal.* 1 (2018) 127–134.
- 5 [11] L. Shen, J. Xu, M. Zhu, Y.-F. Han, *ACS Catal.* 10 (2020) 14581–14591.
- 6 [12] X. Huang, K. Zhang, B. Peng, G. Wang, M. Muhler, F. Wang, *ACS Catal.* (2021)  
7 9618–9678.
- 8 [13] M. Zhu, P. Tian, X. Cao, J. Chen, T. Pu, B. Shi, J. Xu, J. Moon, Z. Wu, Y.-F. Han,  
9 *Appl. Catal. B Environ.* 282 (2021) 119561.
- 10 [14] P. Hongmanorom, J. Ashok, P. Chirawatkul, S. Kawi, *Appl. Catal. B Environ.* 297  
11 (2021) 120454.
- 12 [15] C.J. Pan, M.C. Tsai, W.N. Su, J. Rick, N.G. Akalework, A.K. Agegnehu, S.Y.  
13 Cheng, B.J. Hwang, *J. Taiwan Inst. Chem. Eng.* 74 (2017) 154–186.
- 14 [16] S. Lin, Z. Hao, J. Shen, X. Chang, S. Huang, M. Li, X. Ma, *J. Energy Chem.* 59  
15 (2021) 334–342.
- 16 [17] A. Caballero, J.P. Holgado, V.M. Gonzalez-Delacruz, S.E. Habas, T. Herranz, M.  
17 Salmeron, *Chem. Commun.* 46 (2010) 1097–1099.
- 18 [18] M. Li, H. Amari, A.C. van Veen, *Appl. Catal. B Environ.* 239 (2018) 27–35.
- 19 [19] X. Yuan, T. Pu, M. Gu, M. Zhu, J. Xu, *ACS Catal.* 11 (2021) 11966–11972.
- 20 [20] T.W. van Deelen, C. Hernández Mejía, K.P. de Jong, *Nat. Catal.* 2 (2019) 955–  
21 970.

- 1 [21] G. Kumar, L. Tibbitts, J. Newell, B. Panthi, A. Mukhopadhyay, R.M. Rioux, C.J.  
2 Pursell, M. Janik, B.D. Chandler, *Nat. Chem.* 10 (2018) 268–274.
- 3 [22] M. Tang, S. Li, S. Chen, Y. Ou, M. Hiroaki, W. Yuan, B. Zhu, H. Yang, Y. Gao, Z.  
4 Zhang, Y. Wang, *Angew. Chemie - Int. Ed.* 60 (2021) 22339–22344.
- 5 [23] Ö. Metin, V. Mazumder, S. Özkar, S. Sun, *J. Am. Chem. Soc.* 132 (2010) 1468–  
6 1469.
- 7 [24] M. Zabilskiy, P. Djinović, E. Tchernychova, O.P. Tkachenko, L.M. Kustov, A.  
8 Pintar, *ACS Catal.* 5 (2015) 5357–5365.
- 9 [25] P. Xie, T. Pu, A. Nie, S. Hwang, S.C. Purdy, W. Yu, D. Su, J.T. Miller, C. Wang,  
10 *ACS Catal.* 8 (2018) 4044–4048.
- 11 [26] L. Lin, C.A. Gerlak, C. Liu, J. Llorca, S. Yao, N. Rui, F. Zhang, Z. Liu, S. Zhang,  
12 K. Deng, C.B. Murray, J.A. Rodriguez, S.D. Senanayake, *J. Energy Chem.* 61  
13 (2021) 602–611.
- 14 [27] B. Mutz, P. Sprenger, W. Wang, D. Wang, W. Kleist, J.D. Grunwaldt, *Appl. Catal.*  
15 *A Gen.* 556 (2018) 160–171.
- 16 [28] J.C. Matsubu, S. Zhang, L. DeRita, N.S. Marinkovic, J.G. Chen, G.W. Graham, X.  
17 Pan, P. Christopher, *Nat. Chem.* 9 (2017) 120–127.
- 18 [29] L. Bui, R. Chakrabarti, A. Bhan, *ACS Catal.* 6 (2016) 6567–6580.
- 19 [30] T. Van Herwijnen, H. Van Doesburg, W.A. De Jong, *Appl. Catal. B Environ.* 181  
20 (2016) 504–516.
- 21 [31] R. Mutschler, E. Moioli, W. Luo, N. Gallandat, A. Züttel, *J. Catal.* 366 (2018)

- 1 139–149.
- 2 [32] C. Jia, J. Gao, Y. Dai, J. Zhang, Y. Yang, *J. Energy Chem.* 25 (2016) 1027–1037.
- 3 [33] E.T. Saw, U. Oemar, X.R. Tan, Y. Du, A. Borgna, K. Hidajat, S. Kawi, *J. Catal.*  
4 314 (2014) 32–46.
- 5 [34] J. Ashok, M.L. Ang, S. Kawi, *Catal. Today* 281 (2017) 304–311.
- 6 [35] R.J. Madon, M. Boudart, *Ind. Eng. Chem. Fundam.* 21 (1982) 438–447.
- 7 [36] T. Pu, L. Shen, X. Liu, X. Cao, J. Xu, I.E. Wachs, M. Zhu, *J. Catal.* 400 (2021)  
8 228–233.
- 9 [37] H.C. Wu, Y.C. Chang, J.H. Wu, J.H. Lin, I.K. Lin, C.S. Chen, *Catal. Sci. Technol.*  
10 5 (2015) 4154–4163.
- 11 [38] F. Yang, H. Zhao, W. Wang, L. Wang, L. Zhang, T. Liu, J. Sheng, S. Zhu, D. He,  
12 L. Lin, J. He, R. Wang, Y. Li, *Chem. Sci.* 21 (2021) 12651–12660.
- 13 [39] C. Yang, X. Yu, S. Heißler, A. Nefedov, S. Colussi, J. Llorca, A. Trovarelli, Y.  
14 Wang, C. Wöll, *Angew. Chemie - Int. Ed.* 56 (2017) 375–379.
- 15 [40] S.J. Tauster, *Acc. Chem. Res.* 20 (1987) 389–394.
- 16 [41] L. Fan, J. Zhang, K. Ma, Y. Zhang, Y.M. Hu, L. Kong, A. ping Jia, Z. Zhang, W.  
17 Huang, J.Q. Lu, *J. Catal.* 397 (2021) 116–127.
- 18 [42] N. Wang, W. Qian, W. Chu, F. Wei, *Catal. Sci. Technol.* 6 (2016) 3594–3605.
- 19 [43] M. Kovacevic, B.L. Mojet, J.G. Van Ommen, L. Lefferts, *Catal. Letters* 146 (2016)  
20 770–777.
- 21 [44] R. Mi, D. Li, Z. Hu, R.T. Yang, *ACS Catal.* 11 (2021) 7876–7889.

- 1 [45] F. Wang, C. Li, X. Zhang, M. Wei, D.G. Evans, X. Duan, *J. Catal.* 329 (2015)  
2 177–186.
- 3 [46] C. Cerdá-Moreno, A. Chica, S. Keller, C. Rautenberg, U. Bentrup, *Appl. Catal. B*  
4 *Environ.* 264 (2020) 118546.
- 5 [47] B. Yan, B. Zhao, S. Kattel, Q. Wu, S. Yao, D. Su, J.G. Chen, *J. Catal.* 374 (2019)  
6 60–71.
- 7 [48] M. Németh, F. Somodi, A. Horváth, *J. Phys. Chem. C* 123 (2019) 27509–27518.
- 8 [49] Y. Zhang, X. Yang, X. Yang, H. Duan, H. Qi, Y. Su, B. Liang, H. Tao, B. Liu, D.  
9 Chen, X. Su, Y. Huang, T. Zhang, *Nat. Commun.* 11 (2020) 3185.
- 10 [50] T. Chen, J. Su, Z. Zhang, C. Cao, X. Wang, R. Si, X. Liu, B. Shi, J. Xu, Y.-F. Han,  
11 *ACS Catal.* 8 (2018) 8606–8617.
- 12 [51] Y. Guo, S. Mei, K. Yuan, D.J. Wang, H.C. Liu, C.H. Yan, Y.W. Zhang, *ACS*  
13 *Catal.* 8 (2018) 6203–6215.
- 14 [52] E. Guglielminotti, *Langmuir* 6 (1990) 1455–1460.
- 15 [53] M.D. Rhodes, A.T. Bell, *J. Catal.* 233 (2005) 198–209.
- 16 [54] T. Pu, L. Shen, J. Xu, C. Peng, M. Zhu, *AIChE J.* (2021) 17458.
- 17 [55] Y. Pan, C. Liu, Q. Ge, *J. Catal.* 272 (2010) 227–234.
- 18 [56] K. Feng, J. Tian, M. Guo, Y. Wang, S. Wang, Z. Wu, J. Zhang, L. He, B. Yan,  
19 *Appl. Catal. B Environ.* 292 (2021) 120191.
- 20 [57] X. Jia, X. Zhang, N. Rui, X. Hu, C. jun Liu, *Appl. Catal. B Environ.* 244 (2019)  
21 159–169.

1 [58] J. Zhang, Y. Yang, J. Liu, B. Xiong, Appl. Surf. Sci. 558 (2021) 149866.

2

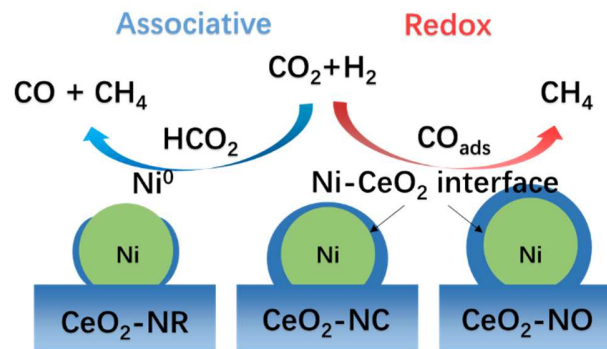
3

4

5

6

TOC Graphics



7

8